https://doi.org/10.5194/egusphere-2026-2129
Preprint. Discussion started: 13 July 2026

Impact of aeolian sediments on the ice-covered lake surface temperature of Zonag Lake, Tibetan Plateau

Jie Gao[1], Guangyin Hu[1], Jingjing Hu[1], Na Gao[1], Zhibao Dong[1]

[1]School of Geography and Tourism, Shaanxi Normal University, Xi'an 710119, China

Correspondence to: Guangyin Hu (guangyinhu@snnu.edu.cn)

Abstract. Aeolian sediments on ice-covered lakes can modify surface energy conditions and potentially influence the thermal environment of lake ice. However, the quantitative relationship between aeolian sediments and lake ice surface temperature remains insufficiently understood. This study investigates the relationship between aeolian sediments and ice-covered lake surface temperature (LST) in Zonag Lake on the Tibetan Plateau using multi-temporal Landsat 8 OLI imagery and MOD11A1 LST data from 2013 to 2018. The Normalized Difference Sandy Land Index (NDSLI) was applied to identify the distribution of aeolian sediments on lake ice. To quantify the sediment impact on LST, spatial regression analyses were conducted using ordinary least squares (OLS), geographically weighted regression (GWR) and multi-scale geographically weighted regression (MGWR). The results show that NDSLI effectively captures the spatial distribution and migration patterns of aeolian sediments on lake ice. Sediment-covered areas (NDSLI < 0) consistently exhibit higher temperature than uncovered areas (NDSLI > 0), with observed temperature differences ranging from 0.83 to 2.36 °C. Finer-scale NDSLI classification indicates a progressive increase in surface temperature with increasing sediment accumulation. Spatial regression results reveal a significant positive relationship between sediment and LST, with MGWR providing the best model performance and explanatory capability among the tested models. This study provides quantitative evidence that aeolian sediment deposition can modify the thermal conditions of lake ice surfaces, offering new insights into cryosphere–aeolian interactions in arid-cold regions and improving the understanding of thermal variability in ice-covered lakes.

1 Introduction

The Tibetan Plateau is known as the "Roof of the World" and the "Asian Water Tower", contained approximately 50,000 km² of lake surface area (for lakes >1 km²) in 2018, representing half of China's total lakes (Qiu et al., 2025; Zhang et al., 2019). However, the unique hydrological regime of this region is closely linked to active aeolian processes (Dong et al., 2017). Several studies indicate that the typical high-wind energy and arid environment of the Tibetan Plateau provides sufficient dynamic conditions for aeolian activities, which play an active role in the formation of sand dunes and aeolian sediments accumulation (Dietze et al., 2014; Dong et al., 2017; Hu et al., 2021; Sun et al., 2007). Especially during the winter and spring seasons, the cold and dry climate conditions combined with frequent strong winds create a high incidence period for aeolian sand transport (Dong et al., 2017; Hu et al., 2013). This period coincides with the seasonal freezing of lakes, some of which remain ice-covered for up to seven months (Liao et al., 2022; Verpoorter et al., 2014; Wu et al., 2022). Such spatiotemporal coupling establishes unique conditions for interactions between aeolian sediments and ice-covered period of lake.

Substantial progress has been made in understanding the thermodynamic effects of externally sourced particulates on snow and ice. Researches confirm that light-absorbing particles (LAPs) such as dust, black carbon (BC), organic carbon (OC), and glacial algae can accelerate ablation through albedo reduction and enhanced shortwave radiation absorption (Cook et al., 2019; Kang et al., 2020; Skiles et al., 2018, 2012; Zhou et al., 2025). Numerical simulations further reveal that LAPs-induced radiative forcing through snow and ice albedo reduction can significantly change regional hydrological processes, including accelerated snowpack ablation, advanced peak runoff timing, and modified precipitation patterns (Qian et al., 2015). This phenomenon exhibits distinct spatial heterogeneity across geographical regions. In the Colorado River Basin of North America, dust has been confirmed as the dominant factor controlling snowpack ablation processes (Skiles et al., 2012). On the Greenland Ice Sheet, glacial algae serve as the primary driver for "dark zone" albedo reduction and ice melt, with their impact surpassing even that of mineral dust (Cook et al., 2019). Observations on the Tibetan Plateau further demonstrate that LAPs significantly reduce snow cover duration (Zhang et al., 2018). Beside these studies, the impacts of aeolian sediments on snow and ice have also attracted significant attention. Observations at Lake Bonney, Antarctica, confirm that aeolian sediments enhance solar radiation absorption, leading to accelerated ice-sheet thinning (Obryk et al., 2014). At Crater Lake in Pangnirtung Pass, Northwest Territories, Canada, winter winds drive aeolian transport and niveo-aeolian deposition onto ice surfaces (Neuman, 1990). On the Tibetan Plateau, the seasonal coupling between aeolian activity and lake ice dynamics is particularly pronounced. At Headwater Region of the Yellow River, extensive aeolian sediments were trapped within ice cracks (Hu et al., 2023). Similarly, Zonag Lake in Hoh Xil shows distinct depositional streaks formed by wind-driven accumulation during the coupling of winter-spring gales with lake freezing periods (Gao et al., 2025). Notably, similar research has extended to planetary science. In Mars, the hypothesized ice-covered paleolake during the Hesperian at Gale Crater provides compelling evidence for interpreting aeolian sediment penetration through ice covers (Kling et al., 2020).

Aeolian sediments in its high-altitude cryosphere of the Tibetan Plateau that not only record atmospheric circulation information but also influence regional climate, glacier ablation, and biogeochemical cycles by changing surface radiation balance (Dong et al., 2020). However, the quantitative mechanism by which aeolian sediments regulate the spatial distribution of lake ice surface temperature remains inadequately supported by systematic research. Elucidating this process carries significant scientific value for understanding cryosphere-aeolian interactions in arid high-altitude regions.

Based on these scientific questions, this study takes Zonag Lake on the Tibetan Plateau as a typical case and applies multi-source remote sensing data and spatial regression analysis methods to systematically investigate the influence mechanism of aeolian sediments on the spatial distribution of lake ice surface temperature. By analyzing the spatial distribution characteristics of aeolian sediments and their thermodynamic effects, this study aims to reveal the key processes of aeolian-cryosphere interactions and provide new theoretical foundations for research on regional climate and environmental changes on the plateau.

https://doi.org/10.5194/egusphere-2026-2129
Preprint. Discussion started: 13 July 2026

2 Study Area

Zonag Lake (91°46'–92°06'E, 35°28'–35°37'N) is located in Hoh Xil region in the interior of the Tibetan Plateau, with an average elevation of 4,800 meters (Fig. 1a). The lake basin has a pear-shaped form due to its geological structure, being wider in the west and narrower in the east (Fig. 1b). This area has a typical high-altitude semi-arid climate. According to observational data (1961-2019) from Wudaoliang Meteorological Station, the area has an annual average temperature of -5.1°C and the mean annual precipitation is 299.8 mm (Chen et al., 2021). Strong winds are frequent, with more than 150 days of wind speeds ≥10.7 m s^{-1} annually, and the dominant wind direction is southwest–west (Xie et al., 2020), providing sustained driving force for aeolian activities.

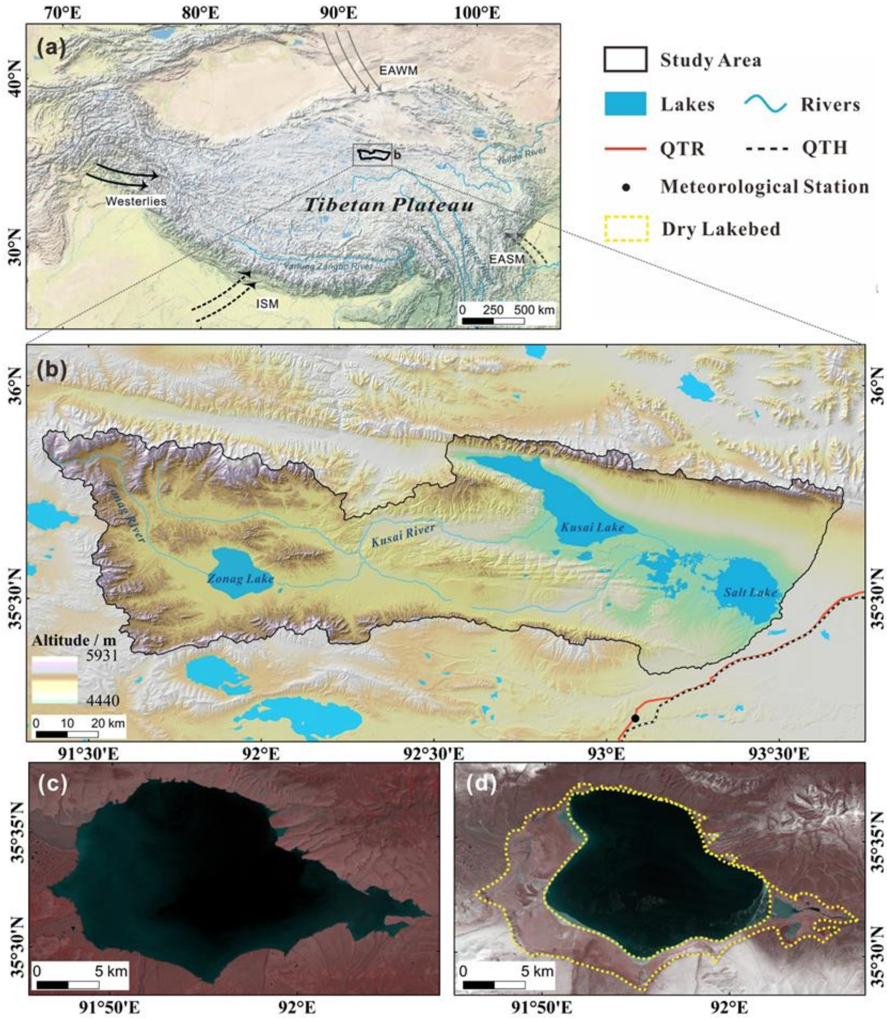

Figure 1. Sketch map of the study area. (a) Location of the Zonag Lake-Salt Lake basin on the Tibetan Plateau; (b) Topographic map of the Zonag Lake-Salt Lake basin; Landsat TM images of August 30, 2009 (c) and November 8, 2011 (d) of Zonag Lake. The area surrounded by the yellow dashed line is the dry lakebed.

https://doi.org/10.5194/egusphere-2026-2129
Preprint. Discussion started: 13 July 2026

In September 2011, the outburst of Zonag Lake triggered a chain reaction of water release, with floodwaters flowing eastward into Kusai Lake, Hedin Noel Lake, and ultimately Salt Lake, forming a new interconnected hydrological system (Yao et al., 2012). Following this event, extensive lakebed exposure occurred along the western and southern shorelines (Fig. 1d), significantly altering regional aeolian conditions Monitoring data revealed that the annual average number of strong wind days during the high-frequency dust storms increased to 31.6 days after 2011, compared with the historical mean of 14.3 days (Lu et al., 2020). Until 2019, the desertification area around the lake had expanded to 600 km². The sediments from the dried lake bed driven by strong winds, continue to migrate, gradually transforming the region into a significant dust source (Xie et al., 2020). Remote sensing analysis indicated that this process has caused grassland degradation covering 470 km², posing severe threats to the fragile plateau ecosystem.

3 Data and Methods

3.1 Data Sources

This study employed a synergistic analysis utilizing LST data and high-resolution remote sensing imagery. The LST data was obtained from the MOD11A1 V6 daily surface temperature of the Terra satellite. This data has a spatial resolution of 1 km and a temporal resolution of 1 day, and can provide extensive surface temperature monitoring information. To examine the influence of aeolian sediments on the thermal distribution across the lake surface, we resampled the acquired LST data to higher resolution (1 km × 1 km) for subsequent analysis. Meanwhile, Landsat 8 Operational Land Imager (OLI) imagery, with a spatial resolution of 30 meters, was employed to facilitate detailed identification of surface features and to compute specialized indices for targeting specific land cover types.

During the data screening process, three key factors were focused on considering. Firstly, images with less than 10% cloud cover should be selected to ensure data quality. Secondly, select images where the lake is in a stable freezing period. Finally, prioritize selecting MODIS and Landsat data acquired on the same day or on close dates. Based on the ice-covered lake period information provided by the "An integrated dataset of daily lake surface temperature over Tibetan Plateau" (Guo et al., 2021), we finally determined 7 sets of time-matched remote sensing image data sets for subsequent analysis (Table 1).

Table 1. Datasets used in this study.

Data source	Date	Resolution /（m）	Description
Landsat 8 OLI	2013-12-30	30	USGS https://earthexplorer.usgs.gov/
	2016-12-07	30	
	2016-12-23	30	
	2017-11-08	30	
	2017-12-26	30	
	2018-01-11	30	
	2018-04-01	30	

https://doi.org/10.5194/egusphere-2026-2129
Preprint. Discussion started: 13 July 2026

	2013-12-31	1000	
	2016-12-08	1000	
	2016-12-20	1000	
MOD11A1 V6	2017-11-07	1000	https://lpdaac.usgs.gov/products/mod11a1v006/
	2017-12-20	1000	
	2018-01-10	1000	
	2018-03-31	1000	

3.2 Methods

3.2.1 Normalized Difference Sandy Land Index (NDSLI)

The NDSLI was initially proposed for extracting sandy areas in arid and semi-arid regions and is applicable to image data such as Landsat TM, ETM+, and OLI 8. It has shown good applicability in related studies (Sahar et al., 2021). In the preliminary work of this study, the effectiveness of this index in identifying aeolian sediments on ice-covered lake was further verified (Gao et al., 2025).

The NDSLI distinguishes sandy areas from other land features by comparing the reflectance of specific bands. It utilizes the sensitivity of the short-wave infrared band (SWIR-1) to humidity and the advantage of the red band (R) in differentiating land types. Since sandy areas typically have low moisture content, their reflectance is higher in the SWIR-1 band, and they also have relatively higher reflectance in the red band, but there are significant differences compared to vegetation or moist soil. These spectral characteristics enable the NDSLI to produce significantly differentiated index values for sandy areas compared to other surfaces, thereby enhancing the accuracy of sandy feature extraction in remote sensing imagery. Generally, sandy areas correspond to lower NDSLI values, while non-sandy surfaces yield values near zero or positive. Based on the above advantages, this study uses NDSLI to conduct spatiotemporal identification and analysis of aeolian sediments on the Zonag Lake. The calculation formula of NDSLI is as follows:

$$NDSLI = \frac{\mathrm{R-SWIR1}}{\mathrm{R+SWIR1}}, \tag{1}$$

where R is the red band (Landsat 8 OLI Band 4) and SWIR1 is the shortwave infrared band (Landsat 8 OLI Band 6). The NDSLI value ranges from -1 to 1.

3.2.2 Spatial Autocorrelation Analysis

Tobler's First Law of Geography states: "Everything is related to everything else, but near things are more related than distant things" (Tobler, 1970). This principle of spatial dependence forms the basis of spatial analysis. For the multi-temporal analysis of individual lake areas in this study, identifying and quantifying spatial relationships is particularly crucial, as it facilitates more effective and accurate modeling of spatial variations in LST.

https://doi.org/10.5194/egusphere-2026-2129
Preprint. Discussion started: 13 July 2026

Among various spatial analysis tools, Moran's I is the most widely used global measure of spatial autocorrelation. It is commonly applied to assess the spatial clustering of residuals from ordinary least squares regression models (Dai et al., 2018). This study utilized ArcGIS and GeoDa software for visualization and analysis. As a key indicator in current spatial statistical analysis, Moran's I is calculated using the following formula (Guo et al., 2020):

$$Moran's\ I = \frac{n\sum_{i=1}^{n}\sum_{j=1}^{n}(x_i-\bar{x})(x_j-\bar{x})}{\sum_{i=1}^{n}\sum_{j=1}^{n}W_{ij}\sum_{i=1}^{n}(x_i-\bar{x})}\ , \tag{2}$$

where n is the number of spatial units; x_i and x_j are the observed values of the variable at locations i and j; $\bar{x}$ is the mean of the observed variable; W_{ij} is the spatial weight between locations i and j.

Additionally, to further explore the local spatial clustering characteristics of LST, this study applied Local Indicators of Spatial Association (LISA) based on the Local Moran's I statistic. The Local Moran's I was computed using the following formula:

$$LocalMoran'sI = (\frac{x_i-\bar{x}}{n})\sum_{i=1}^{n}W_{ij}(x_j-\bar{x})\ , \tag{3}$$

Based on the Local Moran's I results, spatial clustering patterns are categorized into four types: High–High (H–H),Low–Low (L–L),High–Low (H–L), and Low–High (L–H) (Liu et al., 2019).

3.2.3 Ordinary least squares (OLS)

To preliminarily analyze the influence of aeolian sediments on LST, this study first employed OLS regression modeling. As one of the most widely used linear regression methods, OLS estimates the coefficients of independent variables' effects on the dependent variable by minimizing the sum of squared residuals (Malmström & Ekström, 2022). In spatial regression analysis, OLS often serves as a baseline model for comparison with subsequent spatial regression models (Yue et al., 2018). The basic expression of the OLS model is as follows (Park et al., 2021):

$$y = x\beta + \varepsilon\ , \tag{4}$$

where y is a column vector of the dependent variable (i.e., LST), x is a matrix of independent variables (i.e., NDSLI), β represents the regression coefficients， and ε denotes the random error term.

3.2.4 Geographically weighted regression (GWR)

To address the inability of traditional OLS models to capture spatial heterogeneity, this study further employs the GWR model. GWR estimates local regression coefficients for each observation point in geographic space, reflecting spatial variations in the relationship between independent and dependent variables (Dai et al., 2018; Fang et al., 2019; Zhao et al., 2018). This model overcomes the limitation of conventional regression in capturing localized spatial variations, providing a more nuanced spatial characterization of the relationship between LST and aeolian sediments. The specific formula is expressed as:

$$y_i = \beta_0(u_i, v_i) + \sum_k \beta_k(u_i, v_i)\, x_{ik} + \varepsilon_i\ , \tag{5}$$

https://doi.org/10.5194/egusphere-2026-2129
Preprint. Discussion started: 13 July 2026

where v_i is the observed value of the dependent variable at location i; (u_i, v_i) represents the geographic coordinates of observation point i; $\beta_k(u_i, v_i)$ denotes the location-specific regression coefficient for the k-th predictor; ε_i is the residual term. All GWR computations were implemented using MGWR 2.2 software.

3.2.5 Multi-scale geographical weighted regression (MGWR)

Although GWR effectively captures spatial non-stationarity, it assumes a uniform bandwidth for all variables, ignoring scale differences among them (Li et al., 2023). In reality, environmental factors often exhibit multiscale spatial influences, and a single bandwidth may lead to oversimplification or reduced explanatory power (Mansour et al., 2021). To address this limitation, the MGWR method was proposed and gradually improved (Fotheringham et al., 2017). This method makes important improvements on the traditional GWR framework and independently estimates the optimal bandwidth parameter for each explanatory variable, enabling a more accurate reflection of the scale characteristics of the spatial effects of different driving factors (Yu et al., 2023). Its formula is as follows (Fotheringham et al., 2019):

$$y_j = \beta_{bw0}(u_j, v_j) + \sum_k \beta_{bwk}(u_j, v_j)\, x_k + \varepsilon_j \,, \tag{6}$$

where b_w represents the optimal bandwidth for each variable; $\beta_{bw0}(u_j, v_j)$ is the location−specific intercept; $\beta_{bwk}(u_j, v_j)$ is the local regression coefficient for the k−th variable at location j; ε_j is the residual term. All MGWR modeling was performed using MGWR 2.2 software.

4 Results

4.1 Remote sensing identification of aeolian sediments

Based on the visual interpretation of seven typical remote sensing images, this study reveals a significant coupling relationship between aeolian sediments and the ice-covered period of the lake. The observation data shows that after the lake surface freezes, aeolian sediments accumulate on the surface of the ice-covered lake under the driven of the wind to form distinct band-like features (Fig. 2). To verify this phenomenon, we selected images from the non-freezing (Figure 2d) and the snowfall images (Fig. 2g) for comparison. The results show that no obvious sediments accumulation features appeared on the lake surface during these two dates. In the other images of the freezing dates, the band-like distribution of aeolian sediments can be clearly observed, and the extension direction of the sediment bands is consistent with the regional dominant wind direction. Through the analysis of time-series images, it is found that these sediment streaks exhibit obvious spatial migration and morphological evolution characteristics at different times, which reflects the continuous process of sand transport and deposition.
To quantitatively characterize the accumulation features of aeolian sediments, this study systematically calculated the remote sensing images using NDSLI. The extraction results of NDSLI exhibits high consistency with visual interpretation results, and can effectively identify the spatial distribution of aeolian sediments on the ice-covered lake surface. By setting the threshold

https://doi.org/10.5194/egusphere-2026-2129
Preprint. Discussion started: 13 July 2026

of NDSLI < 0, the sediments boundaries can be accurately extracted. Further threshold analysis shows that when NDSLI < -0.15, the extracted boundaries are highly consistent with the boundaries of the most significant sedimentary bands in the images. As the NDSLI value increases, the sediments accumulation intensity gradually decreases (Fig. 2).

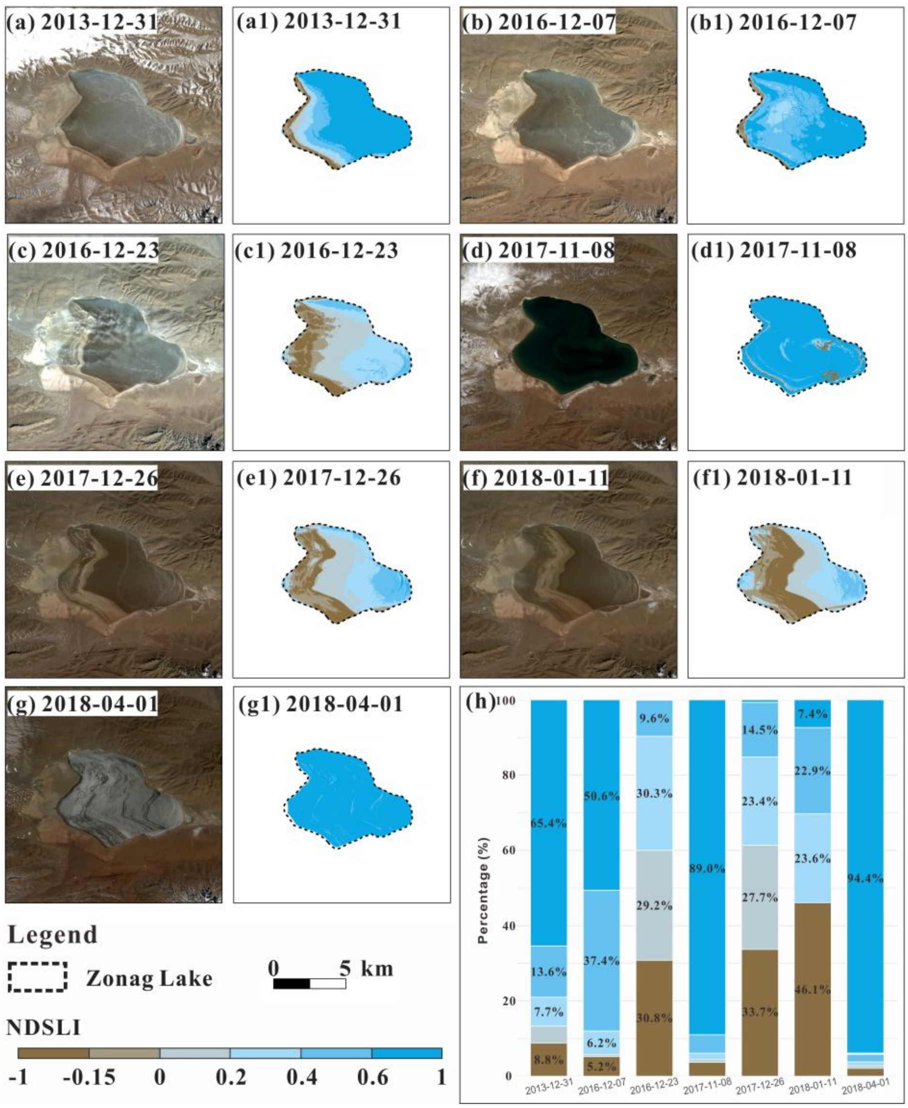

Figure 2. Spatiotemporal distribution of aeolian sediments on the ice-covered lake (a - g) and quantitative analysis of NDSLI based on Landsat 8 OLI imagery. (a1 - g1) Landsat 8 images and corresponding NDSLI calculation results for seven selected dates. (h) Proportions of area classified according to the refined NDSLI grades.

Based on the NDSLI calculation results, we established a spatial distribution vector database for aeolian sediments and calculated the areal percentage corresponding to each threshold interval. Statistical analysis revealed that in images without noticeable sediment accumulation, the proportion of areas with NDSLI < 0 was below 4%. In contrast, images exhibiting obvious sediments showed a substantial increase in this proportion. Specifically, in the image of January 11, 2018, areas with

https://doi.org/10.5194/egusphere-2026-2129
Preprint. Discussion started: 13 July 2026

NDSLI < 0 was accounted for 46.1% of the total lake surface (Fig. 2h). Similarly, on the images of December 26, 2017 and December 23, 2016, the proportion of such areas also exceeded 30% (Fig. 2h). Although continuous time-series analysis of sediments was not conducted in this study, the spatial pattern of aeolian sediments remains evident: under the influence of the prevailing west wind, the degree of sediments accumulation decreases from west to east.

4.3 The spatial distribution characteristics of the LST

The results show that, after minimizing the effects of the lake edge, the LST exhibited notable spatial heterogeneity during aeolian deposition, with certain areas showing significantly higher temperatures than the surrounding (Fig. 3). In contrast, the lake surface temperature during the date without sediment accumulation displayed a relatively uniform distribution pattern, without the occurrence of similar thermal anomalies. This phenomenon is significantly different from the conventional temperature of lake surface, implying that aeolian sediments may change the thermal distribution by modifying the surface properties of the ice-covered lake.

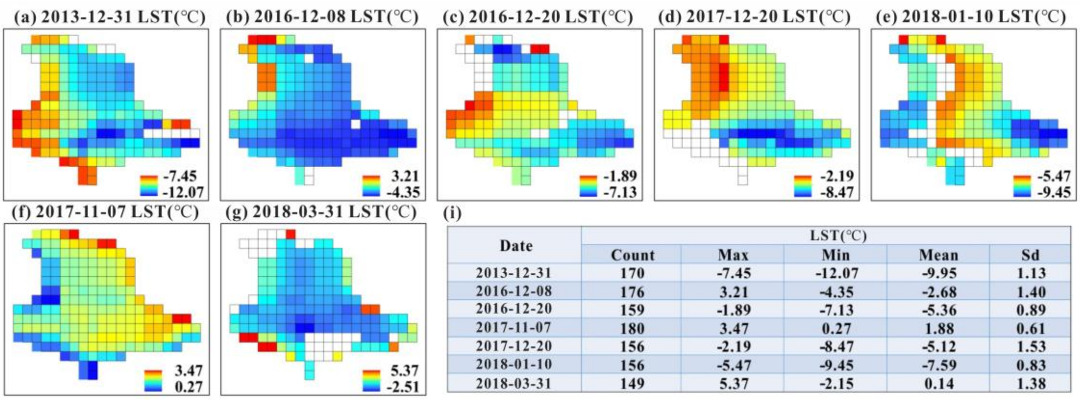

Date	LST(℃)				
	Count	Max	Min	Mean	Sd
2013-12-31	170	-7.45	-12.07	-9.95	1.13
2016-12-08	176	3.21	-4.35	-2.68	1.40
2016-12-20	159	-1.89	-7.13	-5.36	0.89
2017-11-07	180	3.47	0.27	1.88	0.61
2017-12-20	156	-2.19	-8.47	-5.12	1.53
2018-01-10	156	-5.47	-9.45	-7.59	0.83
2018-03-31	149	5.37	-2.15	0.14	1.38

Figure 3. (a-g) Spatial distribution and (i) statistical characteristics of resampled LST data.

4.4. Spatial heterogeneity and clustering patterns of LST

Building upon the preceding analysis that aeolian sediments significantly change the thermal distribution patterns of ice-covered lake surface. To further investigate whether this warming effect exhibits spatial consistency and clustering patterns, this study employs the Global Moran's I and Local Moran's I to quantitatively characterize the spatial structural features of ice-surface temperatures.

The global Moran's I analysis revealed significant spatial autocorrelation in LST across all study dates, with values ranging from 0.3766 to 0.8327 (Fig. 4). During sediment accumulation dates, specifically on November 20, 2017 and January 10, 2018, Moran's I reached 0.8327 and 0.6803, respectively, indicating strong spatial clustering of temperatures. Conversely, during sediment-free dates on April 1, 2018, the index decreased to 0.3766, reflecting more dispersed temperature distributions. These results demonstrate a positive correlation between sediment presence and spatial homogeneity of ice surface temperatures, suggesting that sediment accumulation promotes localized thermal clustering.

https://doi.org/10.5194/egusphere-2026-2129
Preprint. Discussion started: 13 July 2026

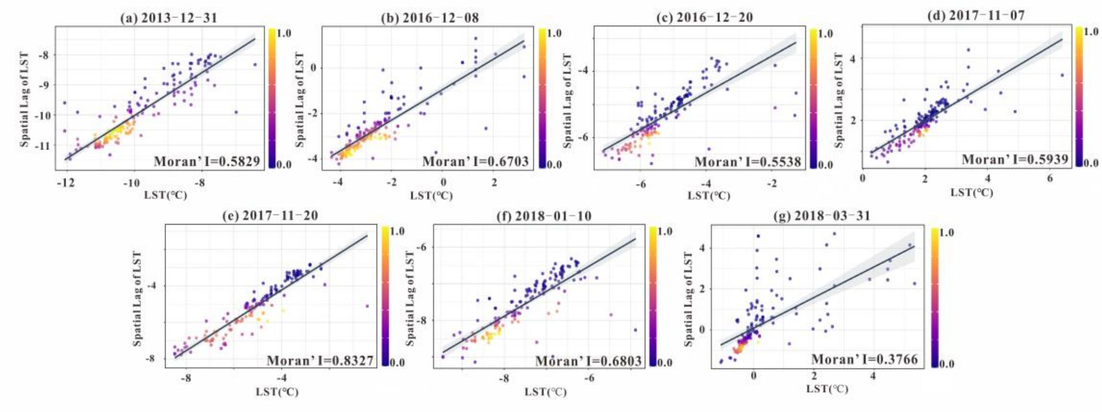

Figure 4. LST Moran's index scatter density maps.

In order to investigate the spatial clustering characteristics and distribution patterns across different regions, LISA analysis was employed to identify local spatial clusters (Fig. 5). The results indicate that high-high (H-H) clusters predominantly occurred in sediment-covered zones, where both focal pixels and their neighborhoods exhibited elevated temperatures, highlighting sediment-driven enhancement of local thermal coherence. Conversely, low-low (L-L) clusters were mainly concentrated in sediment-free or ice areas. Collectively, these findings demonstrate that aeolian sediments not only modify the spatial patterning of surface temperatures but also promote the formation of spatially aggregated thermal zones on ice-covered lakes. This provides critical insight into the mechanisms spatially regulating thermal processes in lacustrine environments.

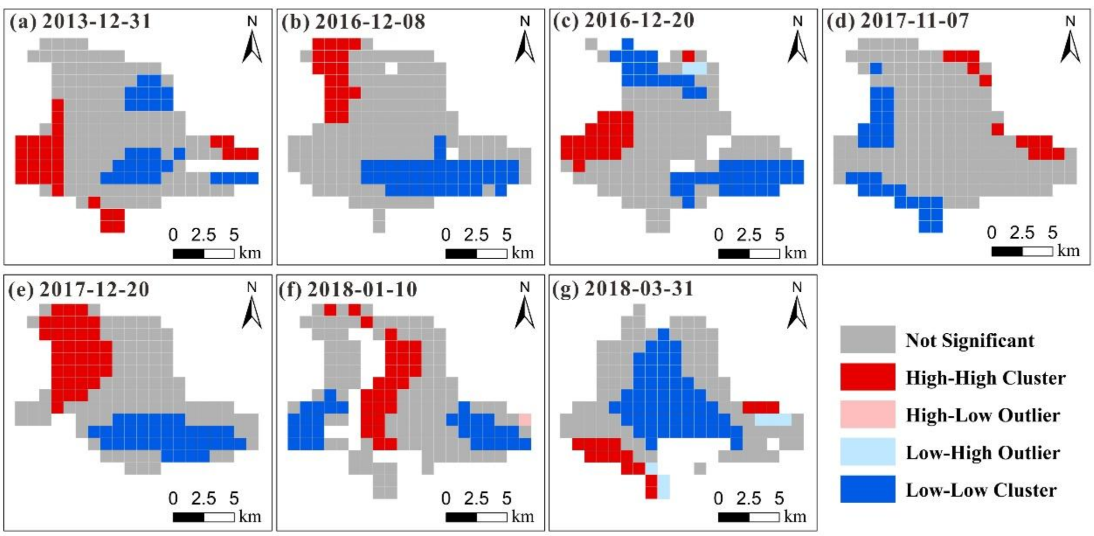

Figure 5. Local spatial autocorrelation distributions.

https://doi.org/10.5194/egusphere-2026-2129
Preprint. Discussion started: 13 July 2026

4.5 Statistical characterization of NDSLI and LST relationship

To further validate this relationship, we selected five typical images of aeolian sediment-covered and performed a spatial overlay analysis between the temperature data and the corresponding NDSLI results (Fig. 6b). The results demonstrate that the areas with more sediment accumulation (characterized by lower NDSLI values) generally exhibited higher temperature values. For instance, the maximum temperature in the sediment-covered area reached -2.19°C on December 20, 2017, while the minimum was -8.47°C in the sediment-free area, resulting in a point-specific temperature difference of 6.28°C. A similar pattern was observed on January 10, 2018, when the maximum temperature in the sediment area reached -5.47°C, which was 3.98°C higher than the minimum temperature of -9.45°C in the sediment-free area. These evidences indicate that the aeolian sediments accumulation significantly changes the thermal distribution of ice-covered lake surface, leading to localized temperature anomalies and consequently disrupting the original spatial pattern of LST.

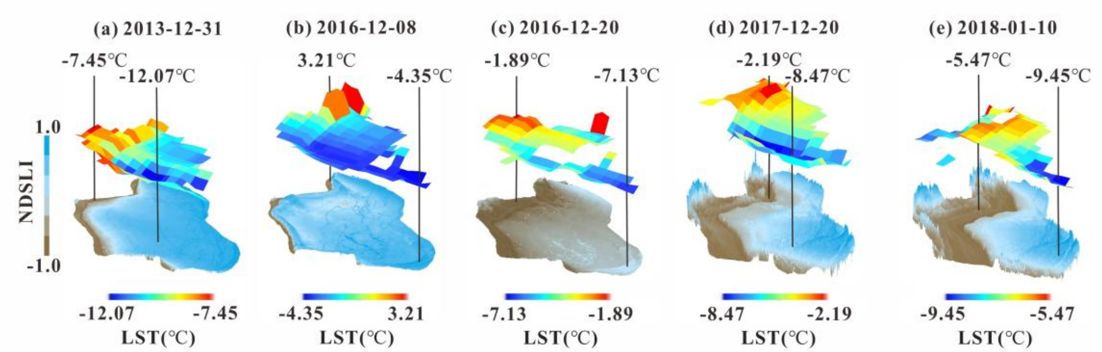

Figure 6. Overlay analysis of LST and NDSLI during typical sediment deposition dates.

Through partitioned statistical analysis of NDSLI and LST across seven dates (Fig. 7a), this study reveals distinct thermal differences between sediment-covered zones (NDSLI < 0) and sediment-free zones (NDSLI > 0). The results indicate that the mean temperature in sediment accumulation zones is consistently higher than in sediments-free zones, with observed temperature differences ranging from 0°C to 2.36°C. Specifically, the maximum temperature difference (2.36°C) was recorded on December 30, 2013, while the minimum difference (0°C) occurred on January 10, 2018. It is noteworthy that the anomalous temperature difference observed on January 10, 2018 may be related to missing values. Excluding this date, the temperature difference range narrows from 0.83°C to 2.36°C. Among all observation dates, December 20, 2017 exhibited the most reliable data quality, showing sediment zones averaging 1.94°C higher than non-sediment zones. Although a larger temperature difference (2.58°C) was observed on March 31, 2018, this result should be interpreted with caution due to limited samples.

https://doi.org/10.5194/egusphere-2026-2129
Preprint. Discussion started: 13 July 2026

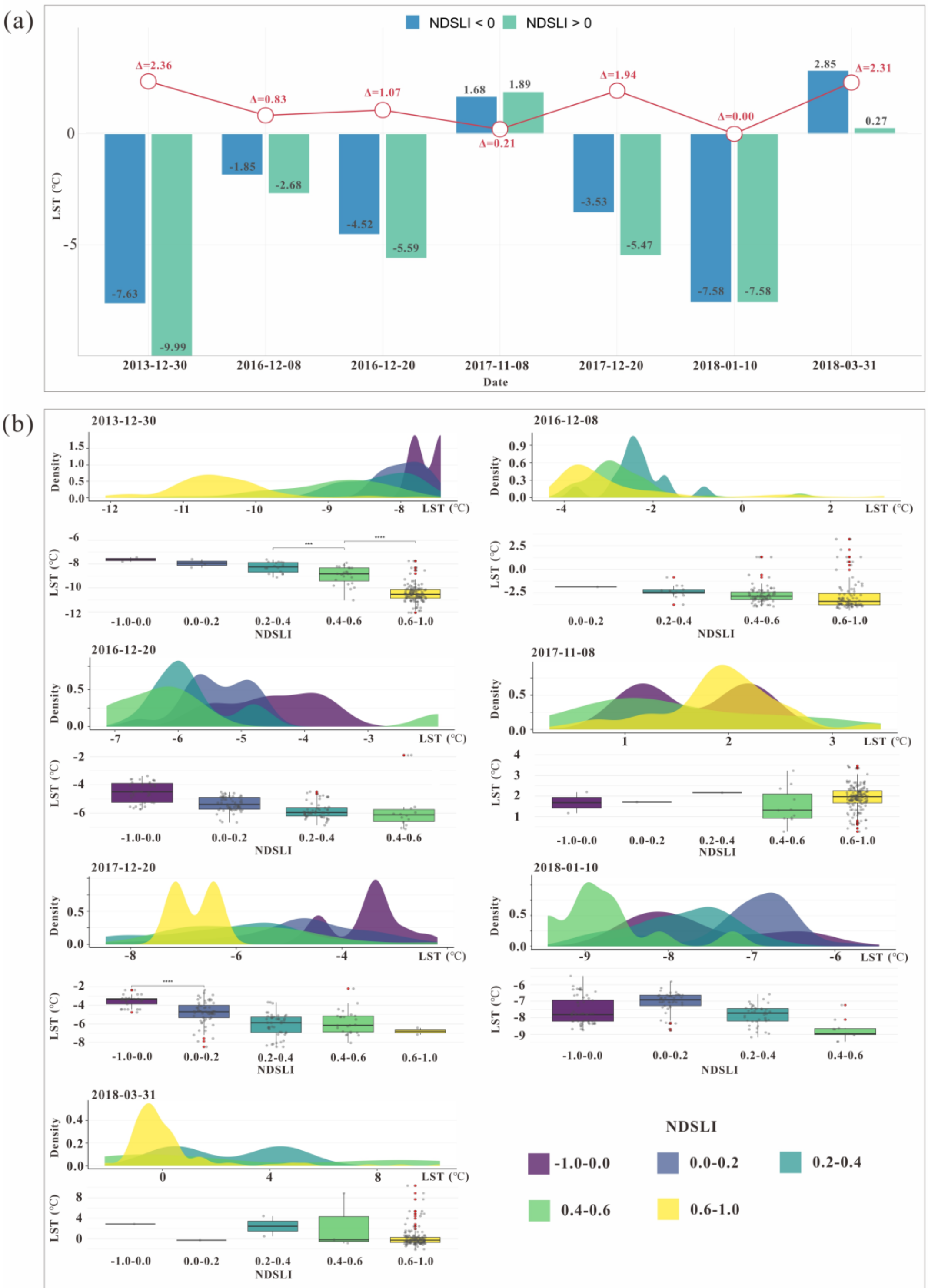

Figure 7. Correlation analysis between LST and NDSLI. (a) Mean LST for areas with NDSLI > 0 and NDSLI < 0, and their difference; (b) KDE and boxplot analysis of LST based on refined NDSLI threshold classifications.

To further investigate the relationship between LST and NDSLI, the study employed a combined approach of kernel density estimation (KDE) and boxplot analysis (Fig. 7b). The KDE results indicate that for the areas with NDSLI < 0, the LST distribution frequently exhibit bimodal pattern, characterized by primary peaks occurring in higher temperature ranges and relatively steep curves, suggesting concentrated temperature distributions. As NDSLI values increase, the peaks of the curves gradually shift toward lower temperatures, and they become broader. Notably, the temperature peaks corresponding to NDSLI < 0 are generally higher than those observed in the NDSLI range of 0.6-1.0. Boxplot analysis further confirms a negative correlation between NDSLI and LST, as evidenced by a decrease in median LST values with increasing NDSLI (Fig. 7b). Among the five observation dates with significant sediment accumulation, all followed this trend except January 10, 2018. These findings demonstrate a clear association between the extent of aeolian sediment accumulation and lake surface thermal conditions: areas with more substantial sediment accumulation tend to form spatially concentrated zones of elevated temperature.

4.4 Regression analysis of NDSLI and LST

Global and Local Moran's I analysis revealed that aeolian sediments accumulation not only change the overall distribution of LST but also enhanced its spatial clustering. To quantify and interpret the driving mechanisms behind this spatial pattern, this study used OLS, GWR, and MGWR models for a multi-level comparative analysis of the spatial relationship between NDSLI and LST.

4.4.1 OLS model results

To preliminarily examine the relationship between aeolian sediment distribution and LST, we constructed an OLS regression model with NDSLI as the independent variable and LST as the dependent variable. The results (Table 2) revealed substantial variations in model performance across different dates. Only one date showed relatively good fitting result (R^2 = 0.567) is December 31, 2013, whereas other dates exhibited poor fitting results with R^2 values all below 0.4. The explanatory power on January 10, 2018 was notably low (R^2 = 0.08), deviating from the expected outcome. With the exception of December 8, 2016 and November 8, 2017, all other observations were statistically significant at the 0.01 level.

Table 2. OLS model regression results.

Date	R^2	Adj-R^2	F-statistic	p-value	AICc
2013-12-31	0.5669	0.5643	219.8609	0.0000*	386.57
2016-12-08	0.0082	0.0025	1.4329	0.2329	620.23
2016-12-20	0.2541	0.2494	53.4855	0.0000*	372.58
2017-11-08	0.1136	0.0058	2.0461	0.1544	337.33
2017-12-20	0.3733	0.3693	91.7471	0.0000*	539.88

https://doi.org/10.5194/egusphere-2026-2129
Preprint. Discussion started: 13 July 2026

2018-01-10	0.0876	0.0816	14.7798	0.0001*	376.94
2018-03-31	0.0369	0.0304	5.6339	0.0189*	625.28

While the OLS model offered a preliminary understanding of the general trend, its assumption of global stationarity limited its ability to capture spatial heterogeneity across different parts of the lake. The presence of spatial autocorrelation in certain residuals, along with the overall weak model performance, suggests that the OLS approach is insufficient for fully explaining the relationship between NDSLI and LST.

4.4.2 GWR model results

The GWR model was applied to examine the localized spatial heterogeneity of the relationship between NDSLI and LST. As summarized in Table 3, the Adj-R^2 values of the GWR model ranged from 0.442 to 0.791 across the seven observation dates, with the highest fitting performance observed on December 20, 2017 (Adj-R^2 = 0.791), followed by January 10, 2018 (Adj-R^2 = 0.708) and December 31, 2013 (Adj-R^2 = 0.689). By contrast, relatively low explanatory power was found on March 31, 2018 (Adj-R^2 = 0.442) and November 8, 2017 (Adj-R^2 = 0.528), suggesting temporal variations in the strength of the NDSLI–LST relationship. Compared with the OLS results, the GWR model provides a more accurate representation of the localized spatial non-stationarity between aeolian sediment distribution and ice-covered lake temperature, as reflected by generally higher Adj-R^2 values and lower AICc.

Table 3. GWR model regression results.

Date	Statistical parameters				
	Bandwidth	R^2	Adj-R^2	AICc	Sigma
2013-12-31	53	0.713	0.689	301.310	0.558
2016-12-08	47	0.704	0.672	326.227	0.573
2016-12-20	46	0.629	0.593	327.348	0.638
2017-11-08	45	0.577	0.528	399.878	0.687
2017-12-20	48	0.809	0.791	217.161	0.457
2018-01-10	46	0.734	0.708	269.610	0.541
2018-03-31	46	0.497	0.442	355.202	0.746

4.4.3 MGWR model results

The MGWR model was further employed to improve upon the limitations of both OLS and GWR by allowing each explanatory variable to operate at its own optimal spatial scale. As shown in Table 4, the Adj-R^2 values ranged from 0.438 to 0.809 across the seven observation dates, consistently outperforming the OLS and GWR results. The highest explanatory power was recorded on December 20, 2017 (Adj-R^2 = 0.809), followed by January 10, 2018 (Adj-R^2 = 0.736) and December 31, 2013 (Adj-R^2 = 0.696). In contrast, the lowest performance occurred on March 31, 2018 (Adj-R^2 = 0.438), suggesting considerable seasonal variability in model effectiveness.

https://doi.org/10.5194/egusphere-2026-2129
Preprint. Discussion started: 13 July 2026

Table 4. MGWR model regression results.

Date	Statistical parameters				
	Bandwidth	R^2	Adj-R^2	AICc	Sigma
2013-12-31	62	0.722	0.696	298.422	0.551
2016-12-08	79	0.708	0.680	318.586	0.565
2016-12-20	44	0.652	0.615	319.364	0.620
2017-11-08	52	0.595	0.552	389.224	0.669
2017-12-20	44	0.827	0.809	204.403	0.473
2018-01-10	44	0.761	0.736	254.922	0.514
2018-03-31	44	0.495	0.438	357.377	0.453

4.4.4 Model performance comparative analysis

A comparative assessment of the OLS, GWR, and MGWR models was conducted by examining their R^2, adjusted R^2, and AICc values across the observation dates (Fig. 8). The results indicate that both GWR and MGWR substantially outperform OLS, demonstrating higher explanatory power and lower AICc values. While OLS is effective in capturing global trends, it fails to reflect spatial heterogeneity. GWR improves upon this limitation by revealing localized sediment–LST relationships, whereas MGWR further enhances model performance through multiscale parameter estimation, striking a better balance between accuracy and parsimony. The superiority of MGWR is particularly evident on dates with extensive sediment coverage, where it achieves the highest fitting accuracy and the most efficient residual control. Overall, MGWR consistently surpasses OLS and GWR, confirming the pivotal role of aeolian sediments in shaping LST heterogeneity and underscoring the strength of MGWR in addressing multiscale geographical processes.

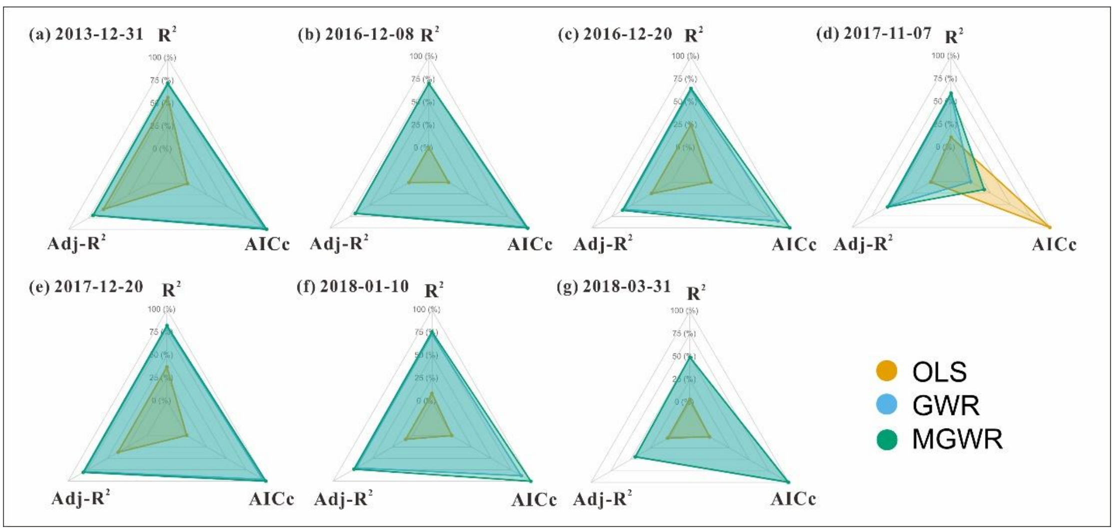

Figure 8. The comparison results of R^2, adj-R^2 and AICc for OSL, GWR and MGWR.

https://doi.org/10.5194/egusphere-2026-2129
Preprint. Discussion started: 13 July 2026

4.4.5 Spatial distribution characteristics of Local R^2 in the MGWR

Building on the comparative analysis, MGWR consistently outperformed OLS and GWR in model fitting and residual control. To further explore spatial heterogeneity, we examined the Local R^2 distribution, which reflects the explanatory power of NDSLI on LST at the local scale (Fig. 9).

The spatial distribution of Local R^2 from the MGWR models across seven dates. High explanatory power (Local $R^2 > 0.80$) appeared mainly on December 20, 2017 and January 10, 2018, forming continuous or clustered hotspots in the central and southern basin, corresponding to periods of strong aeolian activity. Moderate values (0.65–0.80) were observed on December 31, 2013 and December 8, 2016, with localized clusters in the central and southwestern areas, while December 20, 2016 showed only fragmented patches. In contrast, November 7, 2017 and March 31, 2018 were dominated by low values (<0.60), reflecting minimal sediment influence.

In summary, MGWR revealed strong local coupling during peak aeolian activity, with explanatory power concentrated in sediment-rich areas. These results highlight the spatial heterogeneity of sediment–LST interactions and underscore the necessity of multiscale models such as MGWR for accurately characterizing complex lake–sediment–temperature processes.

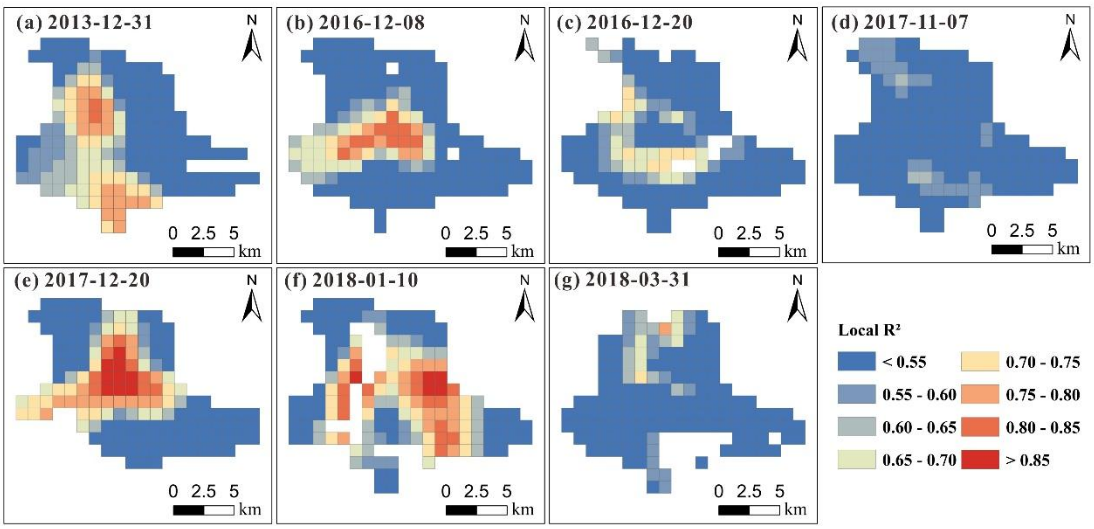

Figure 9. Local-R^2 spatial distributions in MGWR model.

5 Discussion

5.1 Mechanisms underlying the influence of aeolian sediments on LST

The higher LST observed over aeolian sediment–covered zones indicates a distinct thermodynamic perturbation associated with sediment deposition on lake ice. Rather than reflecting a simple reduction in surface albedo alone, this warming signal likely results from a cascade of coupled radiative and thermal processes operating on the ice surface.

https://doi.org/10.5194/egusphere-2026-2129
Preprint. Discussion started: 13 July 2026

Sediment accumulation on lake ice suppresses surface reflectance and enhances shortwave radiation absorption, leading to spatially heterogeneous energy inputs. Analysis of a daily broadband albedo product over the Tibetan Plateau (Wen et al., 2022) for a representative depositional event on 26 December 2017 indicates that sediment-covered ice exhibited a substantially lower mean albedo (~0.10) than adjacent clean ice and snow (~0.52). This albedo contrast with the findings of Dong et al. (2020), who demonstrated that LAPs deposited on snow and ice significantly reduce albedo and induce positive radiative forcing. Although radiative forcing was not explicitly quantified here, the observed albedo anomaly supports a radiatively driven mechanism linking aeolian deposition to LST enhancement.

Consequently, warming over sediment-covered areas generates pronounced spatial heterogeneity in lake ice surface temperature and may influence ice phenology, including the timing and rate of surface melting. To conceptualize this process, we propose a sediment–ice–temperature coupling framework that links sediment release from surrounding surfaces, aeolian transport, deposition onto lake ice, and subsequent thermal responses of the ice surface (Fig. 10). Unlike sloping glacier surfaces, the flat geometry of frozen lakes provides an efficient platform for aeolian accumulation, thereby amplifying its thermodynamic impact. These sediment-induced thermal anomalies may not only modify the spatial distribution of surface temperature but also have broader implications for lake ice evolution and seasonal freeze–thaw dynamics.

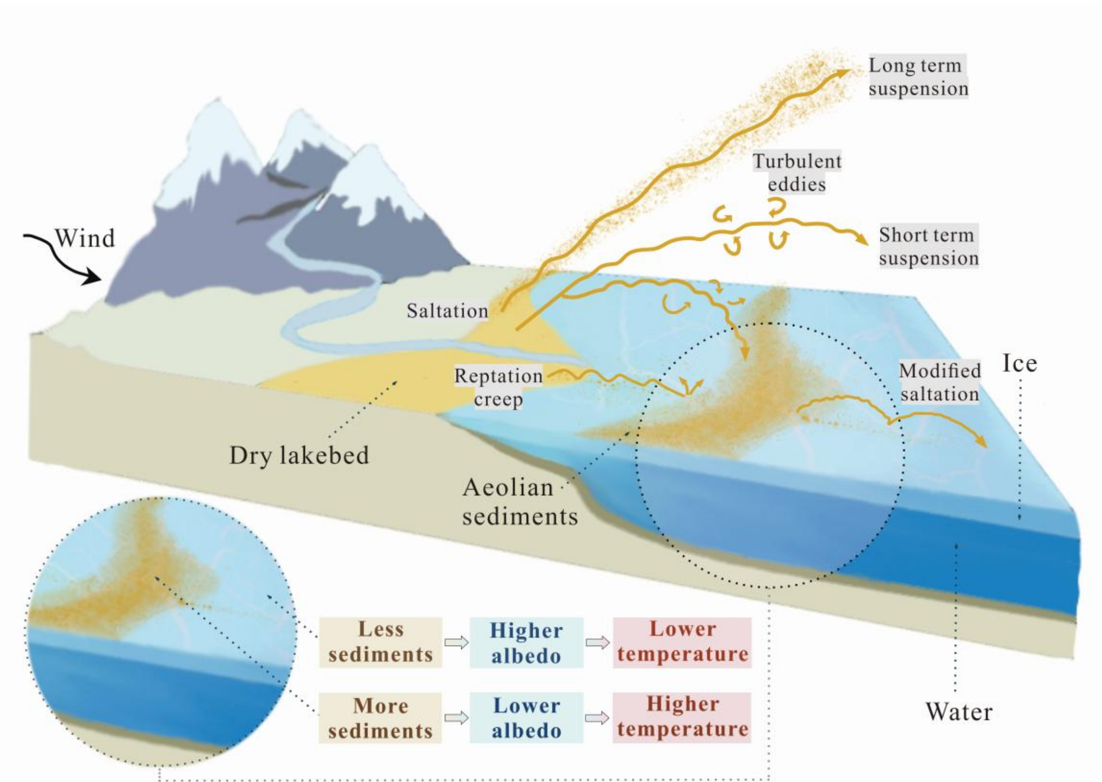

Figure 10. Conceptual model illustrating the coupling between aeolian sediment deposition and ice-covered lake surface warming.

https://doi.org/10.5194/egusphere-2026-2129
Preprint. Discussion started: 13 July 2026

5.2 Implications of aeolian processes for lake ice phenology

Lake ice phenology serves as a critical indicator for characterizing seasonal freeze-thaw cycles of lakes, demonstrating high sensitivity to regional climate change and playing a pivotal role in hydrological processes and ecosystem functioning (Benson et al., 2012; Duguay et al., 2015; Magnuson et al., 2000; Sharma et al., 2019). Global evidence shows that ice duration is shortening, with earlier break-up and delayed freeze-up dates under climate warming (Magnuson et al., 2000; Sharma et al., 2019). However, existing researches have predominantly focused on the combined effects of rising temperatures, enhanced radiation, and lake morphometric characteristics (e.g. area and volume) under climate warming (Benson et al., 2012; Cai et al., 2025; Woolway and Merchant, 2019; Yousefi and Toffolon, 2022), whereas the role of exogenous materials on lake ice surfaces has been largely neglected.

Our results demonstrate that aeolian sediments on lake ice generate persistent hotspots of elevated LST, implying non-negligible consequences for ice phenology. On the Tibetan Plateau, where strong winds frequently coincide with prolonged ice-cover seasons, sediment deposition can substantially modify the surface radiation balance, creating spatially heterogeneous thermal conditions. These localized warming zones may act as preferential sites for early melt initiation or delayed freeze-up, thereby contributing to the shortening of effective ice duration even in the absence of uniform atmospheric warming. Although this study does not directly quantify phenological metrics such as freeze-up or break-up dates, it provides a mechanistic basis for linking surface sediment heterogeneity to large-scale lake ice dynamics.

Similar radiative and thermodynamic mechanisms have been widely documented across other cryospheric components. For example, dust deposition on seasonal snowpacks has been shown to significantly enhance radiative forcing and accelerate snowmelt, reducing snow-cover duration by several weeks (Skiles et al., 2012). Field observations from the Vatnajökull Ice Cap in Iceland indicate that dust deposition can substantially increase snowmelt and contribute a large fraction of seasonal ablation (Wittmann et al., 2017). In alpine regions, mineral dust in snow has also been reported to reduce visible-band reflectance by up to 40%, thereby enhancing solar energy absorption (Di Mauro et al., 2015). These findings collectively highlight the strong capacity of light-absorbing particles to alter surface energy balance and accelerate cryospheric melt processes.

Extending these insights to lake ice systems highlights both similarities and distinctions among cryospheric components. Unlike glaciers or seasonal snowpacks, lake ice is characterized by a relatively flat morphology, direct coupling with the underlying water body, and a strongly seasonal life cycle. These characteristics make lake ice particularly sensitive to localized surface perturbations. Sediment-covered areas disrupt the spatial uniformity of surface temperature, potentially influencing lake–atmosphere heat exchange and the spatial pattern of melt initiation. From a remote sensing perspective, such sediment-induced thermal heterogeneity can be effectively detected through satellite-derived LST products, providing new opportunities to investigate the interactions between aeolian processes and lake ice dynamics in high-altitude environments.

5.3 Limitations

This study has several limitations. First, the relatively coarse temporal resolution of satellite-derived temperature data makes it difficult to capture short-term thermal responses immediately following sediment deposition, which may lead to an underestimation of peak warming effects. Second, although the NDSLI proved effective for mapping sediment coverage, this study did not directly quantify albedo variations or surface energy fluxes, limiting the ability to isolate radiative effects from other thermodynamic processes. Third, the analysis relied on a limited number of high-quality coincident observations of sediment distribution and LST, which may constrain the representation of broader temporal variability. Future studies could address these limitations by integrating higher-temporal-resolution remote sensing data with field observations of radiation and surface temperature. Combining multi-source satellite datasets with process-based modeling would also help clarify the interactions among sediment deposition, radiative forcing, and heat transfer processes. Despite these limitations, this study provides new observational evidence linking aeolian sediment deposition to spatial variations in lake ice surface temperature, highlighting an underexplored pathway through which aeolian processes can influence lake ice thermodynamics.

6 Conclusion

This study combined multi-temporal Landsat 8 and MODIS LST data with the NDSLI and spatial regression models to quantify the thermal impacts of aeolian sediments on ice-covered lakes in the Tibetan Plateau. The main findings are as follows: (1) The NDSLI effectively extracts the distribution of aeolian sediments on ice-covered lake surfaces, revealing pronounced spatial heterogeneity characteristics. (2) Significant thermal differences exist across ice surfaces, with temperatures of sediment-covered areas showing 0.83-2.36°C higher than other areas. (3) Comparative analysis of spatial regression models demonstrates that the MGWR model outperforms conventional OLS and GWR models, achieving determination coefficients (R^2) of 0.65-0.83 during periods of significant sediment accumulation, with local goodness-of-fit exceeding 0.85. These results robustly confirm that sediment coverage serves as a key driver governing the spatial differentiation patterns of LST. Further work using higher-resolution observations and multi-lake analyses will be valuable for improving our understanding of these processes.

Code and data availability

The Landsat 8 Operational Land Imager (OLI) surface reflectance data are available from the U.S. Geological Survey (USGS) EarthExplorer portal (https://earthexplorer.usgs.gov/). The MODIS MOD11A1 land surface temperature product is available from the NASA LP DAAC (https://lpdaac.usgs.gov/products/mod11a1v006/). Spatial regression analyses were conducted with MGWR 2.2 and GeoDa 1.2 (Anselin et al., 2006; Oshan et al., 2019).
All data and software used in this study are publicly available at the sources listed in the References section.

Author contributions

Jie Gao: Conceptualization, Methodology, Software, Formal analysis, Data curation, Writing – original draft, Visualization. Guangyin Hu: Validation, Writing – review & editing, Supervision, Project administration, Funding acquisition. Jingjing Hu: Methodology, Validation, Writing – review & editing. Na Gao: Methodology, Validation, Writing – review & editing. Zhibao Dong: Supervision, Funding acquisition.

Competing interests

The authors declare that they have no conflict of interest..

Acknowledgements

This work was supported by the National Natural Science Foundation of China (Grant nos. 42071004 and 42201005) and the Second Tibetan Plateau Scientific Expedition and Research Program (STEP) (Grant no. 2019QZKK0403).

Financial support

We are grateful for the financial support provided by the National Natural Science Foundation of China (Grant no. 42071004 and 42201005), the Second Tibetan Plateau Scientific Expedition and Research Program (STEP) (Grant no. 2019QZKK0403).

References

Anselin, L., Syabri, I., Kho, Y., 2006. GeoDa : An introduction to spatial data analysis. Geogr. Anal. 38, 5–22. https://doi.org/10.1111/j.0016-7363.2005.00671.x

Benson, B.J., Magnuson, J.J., Jensen, O.P., Card, V.M., Hodgkins, G., Korhonen, J., Livingstone, D.M., Stewart, K.M., Weyhenmeyer, G.A., Granin, N.G., 2012. Extreme events, trends, and variability in northern hemisphere lake-ice phenology (1855–2005). Climatic Change 112, 299–323. https://doi.org/10.1007/s10584-011-0212-8

Cai, Y., Xiao, Y., Shen, X., Li, H., Wang, Z., Wang, J., Ke, C., 2025. Current and projected changes in lake ice phenology on the tibetan plateau: Impacts of climate change and lake expansion. JGR Atmospheres 130. https://doi.org/10.1029/2025jd043623

Chen, Y., Lu, S., Zhou, J., Baig, M.H.A., Chen, F., Tang, H., Zhang, Y., Yang, X., Ge, L., 2021. Hydrological ecosystem changes and impacts after the Zonag Lake outburst in Hoh Xil of Tibetan Plateau. Journal of Asian Earth Sciences: X 6, 100064. https://doi.org/10.1016/j.jaesx.2021.100064

https://doi.org/10.5194/egusphere-2026-2129
Preprint. Discussion started: 13 July 2026

Cook, J.M., Tedstone, A.J., Williamson, C., McCutcheon, J., Hodson, A.J., Dayal, A., Skiles, M., Hofer, S., Bryant, R., McAree, O., McGonigle, A., Ryan, J., Anesio, A.M., Irvine-Fynn, T.D.L., Hubbard, A., Hanna, E., Flanner, M., Mayanna, S., Benning, L.G., Van As, D., Yallop, M., McQuaid, J., Gribbin, T., Tranter, M., 2019. Glacier algae accelerate melt rates on the western greenland ice sheet. https://doi.org/10.5194/tc-2019-58

Dai, Z., Guldmann, J.-M., Hu, Y., 2018. Spatial regression models of park and land-use impacts on the urban heat island in central beijing. Science of The Total Environment 626, 1136–1147. https://doi.org/10.1016/j.scitotenv.2018.01.165

Di Mauro, B., Fava, F., Ferrero, L., Garzonio, R., Baccolo, G., Delmonte, B., Colombo, R., 2015. Mineral dust impact on snow radiative properties in the european alps combining ground, UAV, and satellite observations. JGR Atmospheres 120, 6080–6097. https://doi.org/10.1002/2015JD023287

Dietze, E., Maussion, F., Ahlborn, M., Diekmann, B., Hartmann, K., Henkel, K., Kasper, T., Lockot, G., Opitz, S., Haberzettl, T., 2014. Sediment transport processes across the tibetan plateau inferred from robust grain-size end members in lake sediments. Clim. Past 10, 91–106. https://doi.org/10.5194/cp-10-91-2014

Dong, Z., Brahney, J., Kang, S., Elser, J., Wei, T., Jiao, X., Shao, Y., 2020. Aeolian dust transport, cycle and influences in high-elevation cryosphere of the tibetan plateau region: New evidences from alpine snow and ice. Earth-Science Reviews 211, 103408. https://doi.org/10.1016/j.earscirev.2020.103408

Dong, Z., Hu, G., Qian, G., Lu, J., Zhang, Z., Luo, W., Lyu, P., 2017. High-Altitude Aeolian Research on the Tibetan Plateau. Rev. Geophys. 55, 864–901. https://doi.org/10.1002/2017RG000585

Duguay, C.R., Bernier, M., Gauthier, Y., Kouraev, A., 2015. Remote sensing of lake and river ice, in: Tedesco, M. (Ed.), Remote Sensing of the Cryosphere. Wiley, pp. 273–306. https://doi.org/10.1002/9781118368909.ch12

Fang, L., Li, H., Li, M., 2019. Does hotel location tell a true story? Evidence from geographically weighted regression analysis of hotels in hong kong. Tourism Management 72, 78–91. https://doi.org/10.1016/j.tourman.2018.11.010

Fotheringham, A.S., Yang, W., Kang, W., 2017. Multiscale geographically weighted regression (MGWR). Annals of the American Association of Geographers 107, 1247–1265. https://doi.org/10.1080/24694452.2017.1352480

Fotheringham, A.S., Yue, H., Li, Z., 2019. Examining the influences of air quality in China's cities using multi-scale geographically weighted regression. Transactions in GIS 23, 1444–1464. https://doi.org/10.1111/tgis.12580

Gao, J. et al. (2026) 'Remote sensing monitoring of aeolian sediments on the lake ice surface of Zonag Lake from 2017 to 2018', Journal of Desert Research, (02): 1-10 (in Chinese) .

Guo, A., Yang, J., Sun, W., Xiao, X., Xia Cecilia, J., Jin, C., Li, X., 2020. Impact of urban morphology and landscape characteristics on spatiotemporal heterogeneity of land surface temperature. Sustainable Cities and Society 63, 102443. https://doi.org/10.1016/j.scs.2020.102443

Guo, L., Zheng, H., Wu, Y., Fan, L., Wen, M., Li, J., Zhang, F., Zhu, L., Zhang, B., 2021. An integrated dataset of daily lake surface water temperature over Tibetan Plateau (preprint). Hydrology. https://doi.org/10.5194/essd-2021-151

Hu, G., Dong, Z., Zhang, Z., Yang, L., Hao, L., Hesp, P., Miot Da Silva, G., 2021. Wind regime and aeolian landforms on the eastern shore of qinghai lake, northeastern tibetan plateau, China. Journal of Arid Environments 188, 104451. https://doi.org/10.1016/j.jaridenv.2021.104451

Hu, G., Jin, H., Dong, Z., Lu, J., Yan, C., 2013. Driving forces of aeolian desertification in the source region of the yellow river: 1975–2005. Environ Earth Sci 70, 3245–3254. https://doi.org/10.1007/s12665-013-2389-9

Kang, S., Zhang, Y., Qian, Y., Wang, H., 2020. A review of black carbon in snow and ice and its impact on the cryosphere. Earth-Science Reviews 210, 103346. https://doi.org/10.1016/j.earscirev.2020.103346

Kling, A.M., Haberle, R.M., McKay, C.P., Bristow, T.F., Rivera-Hernández, F., 2020. Subsistence of ice-covered lakes during the hesperian at gale crater, mars. Icarus 338, 113495. https://doi.org/10.1016/j.icarus.2019.113495

Li, D., Zang, H., Yu, D., He, Q., Huang, X., 2023. Study on the influence mechanism and space distribution characteristics of rail transit station area accessibility based on MGWR. IJERPH 20, 1535. https://doi.org/10.3390/ijerph20021535

Liao, F., Wang, G., Yang, N., Shi, Z., Li, B., Chen, X., 2022. Groundwater discharge tracing for a large ice-covered lake in the tibetan plateau: Integrated satellite remote sensing data, chemical components and isotopes (D, 18O, and 222Rn). Journal of Hydrology 609, 127741. https://doi.org/10.1016/j.jhydrol.2022.127741

Liu, C., Wu, X., Wang, L., 2019. Analysis on land ecological security change and affect factors using RS and GWR in the danjiangkou reservoir area, China. Applied Geography 105, 1–14. https://doi.org/10.1016/j.apgeog.2019.02.009

Lu, S., Chen, F., Zhou, J., Hughes, A.C., Ma, X., Gao, W., 2020. Cascading implications of a single climate change event for fragile ecosystems on the Qinghai-Tibetan Plateau. Ecosphere 11, e03243. https://doi.org/10.1002/ecs2.3243

Magnuson, J.J., Robertson, D.M., Benson, B.J., Wynne, R.H., Livingstone, D.M., Arai, T., Assel, R.A., Barry, R.G., Card, V., Kuusisto, E., Granin, N.G., Prowse, T.D., Stewart, K.M., Vuglinski, V.S., 2000. Historical trends in lake and river ice cover in the northern hemisphere. Science 289, 1743–1746. https://doi.org/10.1126/science.289.5485.1743

Mansour, S., Al Kindi, A., Al-Said, Alkhattab, Al-Said, Adham, Atkinson, P., 2021. Sociodemographic determinants of COVID-19 incidence rates in oman: Geospatial modelling using multiscale geographically weighted regression (MGWR). Sustainable Cities and Society 65, 102627. https://doi.org/10.1016/j.scs.2020.102627

Neuman, C.M., 1990. Observations of winter aeolian transport and niveo-aeolian deposition at crater lake, pangnirtung pass, N.W.T., canada. Permafrost & Periglacial 1, 235–247. https://doi.org/10.1002/ppp.3430010304

Obryk, M.K., Doran, P.T., Priscu, J.C., 2014. The permanent ice cover of lake bonney, antarctica: The influence of thickness and sediment distribution on photosynthetically available radiation and chlorophyll-a distribution in the underlying water column: heterogeneity of an antarctic lake. J. Geophys. Res. Biogeosci. 119, 1879–1891. https://doi.org/10.1002/2014JG002672

Oshan, T., Li, Z., Kang, W., Wolf, L., Fotheringham, A., 2019. mgwr: A Python Implementation of Multiscale Geographically Weighted Regression for Investigating Process Spatial Heterogeneity and Scale. IJGI 8, 269. https://doi.org/10.3390/ijgi8060269

https://doi.org/10.5194/egusphere-2026-2129
Preprint. Discussion started: 13 July 2026

Park, Y., Guldmann, J.-M., Liu, D., 2021. Impacts of tree and building shades on the urban heat island: Combining remote sensing, 3D digital city and spatial regression approaches. Computers, Environment and Urban Systems 88, 101655. https://doi.org/10.1016/j.compenvurbsys.2021.101655

Qian, Y., Yasunari, T.J., Doherty, S.J., Flanner, M.G., Lau, W.K.M., Ming, J., Wang, H., Wang, M., Warren, S.G., Zhang, R., 2015. Light-absorbing particles in snow and ice: Measurement and modeling of climatic and hydrological impact. Adv. Atmos. Sci. 32, 64–91. https://doi.org/10.1007/s00376-014-0010-0

Qiu, Y., Chen, J., Chen, D., Woolway, R.I., Luo, H., Xiong, L., 2025. Dipolar response of precipitation to lake expansion on the tibetan plateau. Journal of Hydrology 660, 133532. https://doi.org/10.1016/j.jhydrol.2025.133532

Sharma, S., Blagrave, K., Magnuson, J.J., O'Reilly, C.M., Oliver, S., Batt, R.D., Magee, M.R., Straile, D., Weyhenmeyer, G.A., Winslow, L., Woolway, R.I., 2019. Widespread loss of lake ice around the northern hemisphere in a warming world. Nat. Clim. Chang. 9, 227–231. https://doi.org/10.1038/s41558-018-0393-5

Skiles, S.M., Flanner, M., Cook, J.M., Dumont, M., Painter, T.H., 2018. Radiative forcing by light-absorbing particles in snow. Nature Clim Change 8, 964–971. https://doi.org/10.1038/s41558-018-0296-5

Skiles, S.M., Painter, T.H., Deems, J.S., Bryant, A.C., Landry, C.C., 2012. Dust radiative forcing in snow of the upper colorado river basin: 2. Interannual variability in radiative forcing and snowmelt rates. Water Resources Research 48, 2012WR011986. https://doi.org/10.1029/2012WR011986

Sun, J., Li, S.-H., Muhs, D.R., Li, B., 2007. Loess sedimentation in tibet: Provenance, processes, and link with quaternary glaciations. Quaternary Science Reviews 26, 2265–2280. https://doi.org/10.1016/j.quascirev.2007.05.003

Tobler, W.R., 1970. A computer movie simulating urban growth in the detroit region. Economic Geography 46, 234. https://doi.org/10.2307/143141

Verpoorter, C., Kutser, T., Seekell, D.A., Tranvik, L.J., 2014. A global inventory of lakes based on high-resolution satellite imagery. Geophys. Res. Lett. 41, 6396–6402. https://doi.org/10.1002/2014GL060641

Wen, J., You, D., Han, Y., Lin, X., Wu, S., Tang, Y., Xiao, Q., Liu, Q., 2022. Estimating surface BRDF/albedo over rugged terrain using an extended multisensor combined BRDF inversion (EMCBI) model. IEEE Geosci. Remote Sens. Lett. 19, 1–5. https://doi.org/10.1109/LGRS.2022.3143197

Wittmann, M., Groot Zwaaftink, C.D., Steffensen Schmidt, L., Guðmundsson, S., Pálsson, F., Arnalds, O., Björnsson, H., Thorsteinsson, T., Stohl, A., 2017. Impact of dust deposition on the albedo of vatnajökull ice cap, iceland. The Cryosphere 11, 741–754. https://doi.org/10.5194/tc-11-741-2017

Woolway, R.I., Merchant, C.J., 2019. Worldwide alteration of lake mixing regimes in response to climate change. Nat. Geosci. 12, 271–276. https://doi.org/10.1038/s41561-019-0322-x

Wu, Y., Guo, L., Zhang, B., Zheng, H., Fan, L., Chi, H., Li, J., Wang, S., 2022. Ice phenology dataset reconstructed from remote sensing and modelling for lakes over the tibetan plateau. Sci Data 9, 743. https://doi.org/10.1038/s41597-022-01863-9

https://doi.org/10.5194/egusphere-2026-2129
Preprint. Discussion started: 13 July 2026

Xie, C. et al. (2020) 'Environmental changes caused by the outburst of Zonag Lake and the possible outburst mode of Yanhu Lake in the Hoh Xil region', J. Glaciol. Geocryol., 42(4), pp. 1344–1352 (in Chinese).

Yao, X. et al. (2012) 'Changes of Kusai Lake in Hoh Xil Region and Causes of Its Water Overflowing', Acta Geographica Sinica, 67(5), pp. 689–698 (in Chinese).

Yousefi, A., Toffolon, M., 2022. Critical factors for the use of machine learning to predict lake surface water temperature. Journal of Hydrology 606, 127418. https://doi.org/10.1016/j.jhydrol.2021.127418

Yu, Y., Fang, S., Zhuo, W., 2023. Revealing the driving mechanisms of land surface temperature spatial heterogeneity and its sensitive regions in China based on GeoDetector. Remote Sensing 15, 2814. https://doi.org/10.3390/rs15112814

Yue, Y., Sun, J., Liu, X., Ren, D., Liu, Q., Xiao, X., Lu, L., 2018. Spatial analysis of dengue fever and exploration of its environmental and socio-economic risk factors using ordinary least squares: A case study in five districts of guangzhou city, China, 2014. International Journal of Infectious Diseases 75, 39–48. https://doi.org/10.1016/j.ijid.2018.07.023

Zhang, G., Luo, W., Chen, W., Zheng, G., 2019. A robust but variable lake expansion on the tibetan plateau. Science Bulletin 64, 1306–1309. https://doi.org/10.1016/j.scib.2019.07.018

Zhang, Y., Kang, S., Sprenger, M., Cong, Z., Gao, T., Li, C., Tao, S., Li, X., Zhong, X., Xu, M., Meng, W., Neupane, B., Qin, X., Sillanpää, M., 2018. Black carbon and mineral dust in snow cover on the tibetan plateau. The Cryosphere 12, 413–431. https://doi.org/10.5194/tc-12-413-2018

Zhao, H., Ren, Z., Tan, J., 2018. The spatial patterns of land surface temperature and its impact factors: Spatial non-stationarity and scale effects based on a geographically-weighted regression model. Sustainability 10, 2242. https://doi.org/10.3390/su10072242

Zhou, S., Long, H., Chen, W., Qiu, C., Zhang, C., Xing, H., Zhang, J., Cheng, L., Zhao, C., Cheng, J., Ciais, P., 2025. Temperature seasonality regulates organic carbon burial in lake. Nat Commun 16, 1049. https://doi.org/10.1038/s41467-025-56399-4